Quasilinear Theory of Tokamak Core Transport: Foundations and Validation

Zhifei Gui[1]

Department of Physics and Astronomy, Dartmouth College, Hanover, NH 03755, USA

(*Electronic mail: zhifei.gui.gr@dartmouth.edu)

(Dated: November 10, 2026)

Quasilinear models provide a practical connection between microscopic plasma instabilities and macroscopic transport in tokamak cores. This report reviews their theoretical basis and validation, with emphasis on electrostatic drift-wave turbulence and particle and heat transport. Starting from classical velocity-space quasilinear diffusion, a drift-kinetic derivation traces how equilibrium gradients drive a non-adiabatic response whose phase relative to the electrostatic potential produces radial transport. The gyrokinetic formulation separates transport fluxes into linear response weights, determined by cross-phases and relative fluctuation amplitudes, and a saturated potential spectrum supplied by a separate model. This distinction is essential because local gyrokinetic turbulence can saturate through nonlinear mode coupling before substantial background-profile relaxation occurs. Published mode- and frequency-based quasilinear tests using nonlinear GYRO spectra are examined to assess the response approximation independently of a saturation prescription. These tests support its usefulness for dominant heat-transport scales while identifying limitations associated with strongly inward particle transport and departures from linear amplitude ratios. Comparisons of complete QuaLiKiz flux predictions with nonlinear simulations, DIII-D cross-phase measurements, and JET core-profile predictions illustrate successive levels of validation. Together, these results show how approximately preserved linear responses, combined with a calibrated saturation model, enable efficient transport prediction within a defined range of validity.

Keywords: quasilinear theory, tokamak core transport, gyrokinetic turbulence, drift waves, cross-phase, turbulence saturation

I. REDUCED QUASILINEAR MODELS FOR GYROKINETIC TURBULENT TRANSPORT IN THE CORE

We imphasize the importance of QLT:

1. Quasilinear models are approximately 10^9 times faster than nonlinear simulations and are used for high-fidelity integrated modeling to predict the evolution of temperature, density, and rotation profiles on a timescale of seconds.

2. Neural networks trained based on quasi-linear models are approximately 10^4 times faster, and are used for pulse design across the entire discharge process.

Models of tokamak core transport developed from analytical estimates for individual drift-wave instabilities into models that couple multiple instabilities and transport channels. As gyrokinetic simulations became available, they provided a basis for testing linear mode properties and calibrating turbulent fluxes. Modern reduced quasilinear models combine two ingredients: linear eigenmodes, which determine relative fluctuation amplitudes and cross-phases, and a saturation prescription, which supplies the fluctuation intensity. Their development therefore follows two complementary directions: improving the accuracy and speed of linear calculations, and improving the representation of nonlinear saturation[1]. This framework connects microscopic instability physics to particle and heat transport without resolving the full turbulent evolution. The following discussion develops this connection from classical quasilinear theory and drift-wave response, then examines the approximation through comparisons with nonlinear gyrokinetic simulations.[ZG]

A. Definition of quasilinear

Here, the quasilinear approximation means evaluating the gyrokinetic transport fluxes using linear unstable eigenmodes. For each mode, linear theory determines the complex ratios of density, pressure, and other moment fluctuations to the electric potential fluctuation. These ratios specify both the cross-phases and the relative fluctuation amplitudes, while leaving the overall mode amplitude undetermined. The approximation therefore assumes that these linear response ratios remain representative of the correlations responsible for nonlinear transport, particularly at the scales that dominate the fluxes. A separate saturation prescription is required to determine the potential fluctuation intensity[1].[ZG]

In our lecture, we know continuity equation in v-space:

$$\partial_t F + \partial_v \Gamma_v = 0, \quad \Gamma_v \equiv \frac{q}{m} \langle E \delta f \rangle . \tag{1}$$

so the distribution F changes with flux Γ_v. And we use the linear response δf to calculate the second-order correlation $\langle E \delta f \rangle$. To be more explicit, in fourier expansion, we have linear response

$$\delta f_k \simeq -i \frac{q}{m} \frac{E_k \partial_v F}{\omega_{r,k} - kv + i\gamma_k} \tag{2}$$

so

$$\langle E \delta f \rangle = -\frac{q}{m} \sum_k I_k \frac{\gamma_k}{(\omega_{r,k} - kv)^2 + \gamma_k^2} \partial_v F \tag{3}$$

where $I_k(t) \equiv |E_k(t)|^2$. With defition $\Gamma_v = -D(v)\partial_v F$, we get the diffusion coefficient

$$D(v) = \frac{q^2}{m^2} \sum_k I_k \frac{\gamma_k}{(\omega_{r,k} - kv)^2 + \gamma_k^2} \geq 0 \tag{4}$$

Also in fourier expansion, the evolution equation of the wave is

$$\frac{dE_k}{dt} = (-i\omega_{r,k}[F] + \gamma_k[F]) E_k \tag{5}$$

So there is a circle:

$$F \xrightarrow{\gamma_k[F]} I_k \xrightarrow{D[I_k]} \Gamma_v \xrightarrow{\partial_t F = -\partial_v \Gamma_v} F \tag{6}$$

with the coupled equations which are

$$\partial_t F = \partial_v \left(D[I_k] \partial_v F \right), \quad \frac{dI_k}{dt} = 2\gamma_k[F] I_k. \tag{7}$$

The saturation mechanism for the QLT described above is as follows: waves, through resonant diffusion, flatten the slope of $F(v)$ within the resonance region, causing $\gamma_k[F] \to 0$ and halting the growth of the wave amplitude.

But GK turbulence does not saturate in this mechanism: (i) The step $\Gamma \to F$ is too slow; (ii) the nonlinear terms—which are overlooked in the lecture notes—appear too fast. In particular, in the lecture, we require the time ordering

$$\tau_w \ll t_{\text{eq}} \ll t_{\text{nl}}$$

In other words, the feedback for macropic distribution must be completed before the nonlinear terms of fluctuation come to play. Here we estimate these two times in the tokamak core. We adopt the gyro-Bohm diffusivity $\chi_{\text{GB}} \sim \rho_s^2 c_s / a$, so

$$t_{\text{eq}} \sim \frac{a^2}{\chi_{\text{GB}}} \sim \frac{a}{c_s} \left(\frac{a}{\rho_s} \right)^2 = \frac{a}{c_s} \rho_*^{-2}.$$

Both the growth of turbulence and the nonlinear mixing time are on the order of a/c_s:

$$t_{\rm nl} \sim \gamma^{-1} \sim \frac{a}{c_s}.$$

Consequently,

$$\frac{t_{\rm eq}}{t_{\rm nl}} \sim \rho_*^{-2} \sim 10^4\text{–}10^6,$$

In other words, $t_{\rm nl} \ll t_{\rm eq}$—the exact opposite of what the lecture notes require. Long before any significant change in the background gradient can occur, the nonlinear terms (which the notes discard) have already driven the turbulence to saturation. Gyrokinetic theory separates the time scales associated with turbulent instability and saturation from the slower time scales associated with transport relaxation[1].

So how the system comes to saturate? The saturation by mode coupling is accomplished by a balance between the linear growth and the non-linear mixing by fluctuating $E \times B$ advection[1]

$$\tilde{\mathbf{V}}_{E\times B} \cdot \nabla_\perp \tilde{f} \approx \gamma \tilde{f}. \tag{8}$$

The gyrokinetic ordering requires $\gamma \ll \Omega_i$. Taking $\rho_i \nabla_\perp \sim 1$, it follows from Eq. (8) that $\frac{\tilde{V}_{E\times B}}{v_{ti}} \approx \frac{\gamma}{\Omega_i}$, which means the saturated fluctuation amplitude is of the first order in the small parameter γ/Ω_i. This is the δf ordering[2].

In Staebler *et al.* [1], they noted that "One could say that gyrokinetic turbulence is weak in that it has a small amplitude and preserves the linear eigenmode phase so that the non-linear fluxes can be evaluated by using the linear eigenmodes ..." (Sec. 2.1, p. 4).

B. QL models of GK turbulence

This report mainly discusses the core and local transport of electrostatic drift waves in the closed magnetic surface.

The fact that the perturbation is small relative to the background does not mean that the non-linear terms can be ignored relative to the linear fluctuation dynamics; in the saturation state, the nonlinear coupling can compete with the linear drive, while the phase relationship that dominates the transport still maintains approximately linear characteristics.

a. Linearized gyrokinetic equation Here we omit the standard GK equation and directly start from linearized gyrokinetic equation. The linearized gyrokinetic equation, for a single frequency

ω electric potential fluctuation ($\delta\phi = \tilde{\phi}e^{-i\omega t+iS}, \delta g_a = \tilde{g}_a e^{-i\omega t+iS}$),can be written in the form[3]

$$\begin{aligned} &-i\left(\omega - u_{||}\omega_{k||} - u_{||}^2\omega_{d||} - u_{\perp}^2\omega_{d_\perp}\right)\tilde{g}_a + \langle C_a^{\text{lin}}\rangle_\alpha \\ &= -i\left(\omega - \omega_{n_a} - \omega_{T_a}\left(\frac{u^2}{2} - \frac{3}{2}\right)\right) J_0\left(b_a\right)\frac{e_a\bar{\phi}}{T_a}F_a. \end{aligned} \tag{9}$$

Here, $u = v/v_{ta}$; $\omega_{k_\parallel}$ corresponds to parallel flow; $\omega_{d_\parallel}$ and $\omega_{d_\perp}$ are the drift frequencies arising from magnetic field curvature and gradients; ω_{n_a} and ω_{T_a} are the diamagnetic drift frequencies associated with equilibrium density and temperature gradients; and $J_0(b_a)$ originates from gyrophase averaging, representing finite Larmor radius effects. The system of equations is closed by the quasineutrality condition $\sum_a e_a\tilde{n}_a = 0$.

- LHS is the resonance operator; resonance occurs when the parallel motion and magnetic drift of a particle match the wave frequency—this corresponds to the expression $\omega - kv$ found in the lecture.

- RHS represents the drive: the free energy originates from the spatial gradients ω_{n_a} and ω_{T_a}, rather than from the velocity-space gradient $\partial_v F$ mentioned in the lecture.

b. Flux formula The radial $E\times B$ velocity resulting from the fluctuating potential is

$$\frac{c\,\mathbf{B}\times\nabla\tilde{\phi}\cdot\nabla r}{c_0 B^2} = ik_y\frac{e\tilde{\phi}}{T_0}. \tag{10}$$

The radial particle flux is

$$\Gamma_a = \sum_{k_x}\sum_{k_y} c_0\left\langle \text{Re}\left[ik_y\frac{e\tilde{\phi}^*_{k_x,k_y}}{T_0}\tilde{n}_{a,k_x,k_y}\right]\right\rangle_{t,\theta}, \tag{11}$$

The flux .Eq. (11) arises from the correlation between $\tilde{n}$ and the radial $E\times B$ velocity; only the component of $\tilde{n}$ that has a phase difference relative to $\tilde{\phi}$ contributes to net transport. It's interesting to compare it with Γ_v defined in Eq. (1). Both are derived from the phase-space transport equation. Let f denote the background distribution and δf the fluctuation; then,

$$\partial_t f + \nabla_\alpha\cdot\Gamma_\alpha = 0, \quad \Gamma_\alpha = \langle\tilde{u}_\alpha\,\delta f\rangle,$$

where α represents a specific coordinate, and $\tilde{u}_\alpha$ is the fluctuating velocity component along that coordinate. For QLT, set $\alpha = v$ and $\tilde{u}_v = qE/m$, which yields

$$\Gamma_v = \frac{q}{m}\langle E\,\delta f\rangle.$$

For gyrokinetics, set $\alpha = r$ and $\tilde{u}_r = v_{E,r}$, which yields

$$\Gamma_a = \langle\tilde{n}_a\,v_{E,r}\rangle.$$

c. Specific form of the QL approximation Using Eq. (9), and the density moment of the linear fluctuating distribution function is given by

$$\tilde{n}_{a,k_y} = -\frac{e_a n_a}{T_a}\tilde{\phi}_{k_y} + \frac{2\pi}{m_a^2}\sum_\sigma \int d\varepsilon \frac{B d\mu}{|v_\parallel|} J_0(b_a)\tilde{g}_{ak_y}. \tag{12}$$

The first term is the adiabatic part, and the second term is the non-adiabatic part. And substitute Eq. (12) into the radial flux (Eq. (11)), only the non-adiabatic term remains, and we get an extreme looooooong formula in QL approximation, i.e.

$$\Gamma_{ak_y}^{QL} = \frac{1}{n_a \left\langle \left| \frac{e\tilde{\phi}_{k_y}}{T_0} \right|^2 \right\rangle_\theta} \left\langle \mathrm{Re}\left[ik_y \frac{e\tilde{\phi}_{k_y}^*}{T_0} \frac{2\pi}{m_a^2} \sum_\sigma \int d\varepsilon \frac{B d\mu}{|v_\parallel|} J_0(b_a)\tilde{g}_{ak_y} \right] \right\rangle_\theta, \tag{13}$$

which is called "quasilinear weights". QL approximation assumes that cross-terms between different k_y modes vanish upon time averaging, leaving only the contributions from each individual mode. Consequently, the total flux is

$$\Gamma_a^{QL} = \Gamma_{GB} \sum_{k_y} \Delta k_y I_{k_y}^{QL} \Gamma_{ak_y}^{QL}. \tag{14}$$

$I_{k_y}^{QL}$ is the saturated potential intensity for a given k_y; Δk_y is the spectral bin width; $\Gamma_{GB} = n_0 c_0 (\rho_0/L_0)^2$ provides the correct dimensions.

C. Saturation rules and model construction

The quasilinear weights encode the linear cross-phases and amplitude ratios, but quasilinear theory does not determine the saturated amplitude. Since there is no rigorous theory of gyrokinetic saturation, saturation models are physics-constrained fits: the intensity is a function of the linear spectrum only, and the coefficients are calibrated against nonlinear gyrokinetic fluxes[1]. The simplest example is QuaLiKiz[4], which sets

$$D_{\mathrm{QL}} = C_{\mathrm{NL}} \left. \frac{\gamma_k}{k_\perp^2} \right|_{\max}, \tag{15}$$

This mixing-length scaling follows from $k_\perp^2 D \sim \gamma$, i.e. the balance between linear growth and $E \times B$ mixing of Eq. (8) at fixed gradients, with a spectral shape S_k taken from nonlinear simulations and reflectometry. Because C_{NL} is calibrated on the heat flux alone, the ratios between transport channels remain set by the quasilinear weights. Zonal flows enter this saturation prescription only implicitly through C_{NL} and S_k.

a. From local fluxes to profile evolution. The resulting quasilinear fluxes provide a closure for the slower transport evolution. For example, in a fixed magnetic geometry, flux-surface-averaged particle conservation takes the form

$$\frac{\partial n_a}{\partial t} + \frac{1}{V'}\frac{\partial}{\partial r}\left[V'\left(\Gamma_a^{\mathrm{QL}} + \Gamma_a^{\mathrm{neo}}\right)\right] = S_a, \qquad V' = \frac{dV}{dr}. \tag{16}$$

Here, $V(r)$ is the volume enclosed by a magnetic surface, S_a is the particle source, and Γ_a^{neo} is the neoclassical particle flux. The density and source are flux-surface averages, and each radial flux is defined as $\Gamma_a = \langle \boldsymbol{\Gamma}_a \cdot \nabla r \rangle$. The quasilinear flux is evaluated from the local profiles and their gradients. Together with energy and momentum balance equations, initial and boundary conditions, this closes the profile-evolution problem. Such coupling to transport solvers is the basis of the integrated modelling applications reviewed in Staebler *et al.* [1], Secs. 5.1–5.2.[ZG]

II. TRANSPORT IN DRIFT KINETICS: AN ILLUSTRATION

Here, we use a relatively simple slab drift wave model to clearly derive the mechanism by which the response translates into flux.

Let (x, y, z) are radial coordinate, coordinate in the magnetic surface perpendicular to the magnetic field, and coordinate along the magnetic field direction. The background magnetic field is approximated as $\mathbf{B} = B\hat{\mathbf{z}}$, and the equilibrium distribution is written as

$$F_{0s}(x, \mathbf{v}) = n_{0s}(x)\left(\frac{m_s}{2\pi T_s(x)}\right)^{3/2} \exp\left[-\frac{m_s v^2}{2T_s(x)}\right]. \tag{17}$$

In the lecture, we already know the drift-kinetic equation[5]

$$\frac{\partial f_s}{\partial t} + \mathbf{v}_E \cdot \nabla_\perp f_s + v_\parallel \frac{\partial f_s}{\partial z} - \frac{e}{m_s} E_\parallel \frac{\partial f_s}{\partial v_\parallel} = 0, \quad \mathbf{v}_E = \frac{\mathbf{E}\times\mathbf{B}}{B^2}. \tag{18}$$

Integrating Eq. (18) over velocity yields the electron continuity equation:

$$\frac{\partial n_e}{\partial t} + \nabla_\perp \cdot (n_e \mathbf{v}_E) + \frac{\partial}{\partial z}(n_e u_z) = 0. \tag{19}$$

Define the averaging operator as

$$\langle \cdots \rangle = (L_y L_z)^{-1} \int dy\, dz.$$

Since the total derivative along a periodic direction averages to zero, the ∂_y and ∂_z terms vanish. We decompose the density as $n_e = n_0(x,t) + \tilde{n}$. In the equilibrium state, there is no electric field;

thus, $v_{Ex} = \tilde{v}_x$, and $\langle n_0 \tilde{v}_x \rangle = n_0 \langle \tilde{v}_x \rangle = 0$. Consequently, we have

$$\frac{\partial n_0}{\partial t} = -\frac{\partial \Gamma}{\partial x}, \qquad \Gamma \equiv \langle \tilde{n}\, \tilde{v}_x \rangle. \tag{20}$$

If $\tilde{n}, \tilde{v}_x = O(\varepsilon)$, then $\Gamma = O(\varepsilon^2)$. The background profile evolves on a slow time scale of $O(\varepsilon^{-2})$, while Γ can be calculated using first-order linear solutions.

Consider wave-like perturbations of this equilibrium in which components of the **k**-vector are allowed in the y and z directions, so that any perturbation quantity ψ can be written[5]

$$\psi(\mathbf{x}, t) = \hat{\psi}(x) \exp(-i\omega t + ik_y y + ik_z z) \tag{21}$$

where $\hat{\psi}$ denotes the amplitude of the perturbed quantity ψ. The perturbation quantity should be taken as its real part: $A = \mathrm{Re}[\hat{A} e^{i\theta}]$, where $\theta = k_y y + k_z z - \omega t$. Since $e^{i\theta} = e^{i(k_y y + k_z z - \omega_r t)} e^{\gamma t}$, we have

$$AB = \tfrac{1}{4} \left(\hat{A} e^{i\theta} + \hat{A}^* e^{-i\theta^*} \right) \left(\hat{B} e^{i\theta} + \hat{B}^* e^{-i\theta^*} \right).$$

Upon averaging over y and z, the terms containing $e^{\pm 2i(k_y y + k_z z)}$ vanish, leaving only the cross-terms:

$$\langle AB \rangle = \tfrac{1}{2} \mathrm{Re}(\hat{A} \hat{B}^*)\, e^{2\gamma t}.$$

From $\mathbf{E} = -\nabla \phi$, it follows that $\hat{E}_y = -ik_y \hat{\phi}$ and $\hat{E}_z = -ik_z \hat{\phi}$. Given $\mathbf{B} = B\hat{z}$, we have $(\mathbf{E} \times \mathbf{B})_x = E_y B$; thus,

$$\hat{v}_x = \frac{\hat{E}_y}{B} = -\frac{ik_y \hat{\phi}}{B}. \tag{22}$$

Applying the averaging rule:

$$\boxed{\Gamma = \tfrac{1}{2} \mathrm{Re}(\hat{n} \hat{v}_x^*) = \tfrac{1}{2} \mathrm{Re}\left(\frac{ik_y}{B} \hat{n} \hat{\phi}^* \right) = -\frac{k_y}{2B} \mathrm{Im}(\hat{n} \hat{\phi}^*) = -\frac{k_y}{2B} |\hat{\phi}|^2 \, \mathrm{Im}\left(\frac{\hat{n}}{\hat{\phi}} \right).} \tag{23}$$

And also there is phase difference $\hat{n}/\hat{\phi} = |\hat{n}/\hat{\phi}| e^{-i\alpha}$. So we find

$$\boxed{\Gamma = \frac{k_y}{2B} |\hat{n}| |\hat{\phi}| \sin \alpha} \tag{24}$$

Also we start from Eq. (18) to get linear rsponse of rlectrons. Write $f_e = f_{e0}(x, \mathbf{v}) + f_{e1}$. Since f_{e0} depends only on x, the $\mathbf{E} \times \mathbf{B}$ term reduces to $(E_y/B) \partial_x f_{e0}$. Retaining first-order quantities yields

$$-i(\omega - k_z v_z) \hat{f}_{e1} + \frac{\hat{E}_y}{B} \frac{\partial f_{e0}}{\partial x} - \frac{e}{m} \hat{E}_z \frac{\partial f_{e0}}{\partial v_z} = 0. \tag{25}$$

For the Maxwellian distribution given by Eq. (17), assuming T_e is constant, there are two derivatives:

$$\frac{\partial f_{e0}}{\partial x} = \frac{f_{e0}}{n_0}\frac{dn_0}{dx} = -\frac{eBv_{de}}{T_e}f_{e0}, \qquad \frac{\partial f_{e0}}{\partial v_z} = -\frac{mv_z}{T_e}f_{e0}. \tag{26}$$

Substituting $\hat{E}_y = -ik_y\hat{\phi}$ and $\hat{E}_z = -ik_z\hat{\phi}$, we calculate the terms individually:

- Second term: $\dfrac{-ik_y\hat{\phi}}{B}\Big(-\dfrac{eBv_{de}}{T_e}\Big)f_{e0} = +i\dfrac{e\hat{\phi}}{T_e}k_y v_{de} f_{e0}$
- Third term: $-\dfrac{e}{m}(-ik_z\hat{\phi})\Big(-\dfrac{mv_z}{T_e}\Big)f_{e0} = -i\dfrac{e\hat{\phi}}{T_e}k_z v_z f_{e0}$

So we get

$$-i(\omega - k_z v_z)\hat{f}_{e1} + i\frac{e\hat{\phi}}{T_e}f_{e0}\,(k_y v_{de} - k_z v_z) = 0, \tag{27}$$

and

$$\hat{f}_{e1} = \frac{e\hat{\phi}f_{e0}}{T_e}\,\frac{\omega_* - k_z v_z}{\omega - k_z v_z} = \frac{e\hat{\phi}f_{e0}}{T_e}\Big[1 - \frac{\omega - \omega_*}{\omega - k_z v_z}\Big]. \tag{28}$$

The electron density perturbation is obtained by integrating Eq. (28) over all velocities, giving

$$\hat{n}_e = \frac{n_0 e\hat{\phi}}{T_e}[1 - (\omega - \omega_*)\mathscr{I}], \quad \mathscr{I} \equiv \frac{1}{n_0}\int_{-\infty}^{\infty}\frac{F_{e0}(v_z)dv_z}{\omega - k_z v_z}. \tag{29}$$

$\omega_* \equiv k_y v_{de}$ is the drift frequency. By calculate the contour integral, we have

$$\hat{n}_e = \frac{n_0 e\hat{\phi}}{T_e}\Big[1 + i\sqrt{\frac{\pi}{2}}\,\frac{\omega - \omega_*}{|k_z|v_{t,e}}\Big] \equiv \frac{n_0 e\hat{\phi}}{T_e}(1 - i\delta), \qquad \delta = \sqrt{\frac{\pi}{2}}\,\frac{\omega_* - \omega}{|k_z|v_{t,e}}. \tag{30}$$

At first order, ω in δ is taken as its real part ω_r; therefore, δ is a real number. We already know from Eq. (30) that $\mathrm{Im}\Big(\frac{\hat{n}_e}{\hat{\phi}}\Big) = -\frac{n_0 e}{T_e}\delta$, insert it into Eq. (23)

$$\Gamma = -\frac{k_y}{2B}|\hat{\phi}|^2\Big(-\frac{n_0 e}{T_e}\delta\Big) = \frac{n_0 k_y}{2B}\frac{e|\hat{\phi}|^2}{T_e}\sqrt{\frac{\pi}{2}}\,\frac{\omega_* - \omega_r}{|k_z|v_{t,e}}. \tag{31}$$

The cold-ion fluid response is given by[5]:

$$\hat{n}_i = \frac{n_0 e\hat{\phi}}{T_e}\left(\frac{\omega_*}{\omega} + \frac{k_z^2 C_s^2}{\omega^2} - k_\perp^2\rho_s^2\right). \tag{32}$$

Applying quasineutrality, $\hat{n}_e = \hat{n}_i$, and cancelling the common factor gives

$$1 - i\delta = \frac{\omega_*}{\omega} + \frac{k_z^2 C_s^2}{\omega^2} - k_\perp^2\rho_s^2. \tag{33}$$

Multiplying both sides by ω and rearranging yields

$$\boxed{\omega(1 + k_\perp^2\rho_s^2) - \omega_* - \frac{k_z^2 C_s^2}{\omega} = i\omega\delta.} \tag{34}$$

Writing this as $L(\omega) = i\omega\delta$, we expand the complex frequency as $\omega = \omega_r + i\gamma$, with $|\gamma| \ll |\omega_r|$, to obtain the relation between δ and γ. Expanding to first order in γ gives $L(\omega_r) + i\gamma L'(\omega_r) = i\omega_r\delta$. The real part gives $L(\omega_r) = 0$, yielding $\omega_r \simeq \omega_*(1 - k_\perp^2\rho_s^2) + k_z^2 C_s^2/\omega_*$ [GR(26.36)]. For the imaginary part, $L' = 1 + k_\perp^2\rho_s^2 + k_z^2 C_s^2/\omega_r^2 \simeq 1$, so

$$\gamma \simeq \omega_r\,\delta \quad \Longleftrightarrow \quad \delta = \frac{\gamma}{\omega_r}. \tag{35}$$

Substituting $\omega_* - \omega_r \simeq \omega_*\left(k_\perp^2\rho_s^2 - k_z^2 C_s^2/\omega_*^2\right)$ back into the expression gives the growth rate

$$\gamma = \left(\frac{\pi}{2}\right)^{1/2} \frac{k_y^2 v_{\mathrm{de}}^2}{|k_z| v_{\mathrm{t,e}}} \left(k_\perp^2 r_{\mathrm{Ls}}^2 - \frac{k_z^2 C_s^2}{k_y^2 v_{\mathrm{de}}^2}\right). \tag{36}$$

Substituting $\delta = \gamma/\omega_r$ into Eq. (31) gives

$$\Gamma = \frac{n_0 k_y}{2B} \frac{e|\hat{\phi}|^2}{T_e} \frac{\gamma}{\omega_r}. \tag{37}$$

From $\omega_* = -\dfrac{k_y T_e}{n_0 eB}\dfrac{dn_0}{dx}$, we obtain $\dfrac{e}{T_e} = -\dfrac{k_y}{n_0 B\omega_*}\dfrac{dn_0}{dx}$. Substituting this gives

$$\Gamma = -\frac{k_y^2|\hat{\phi}|^2}{2B^2} \frac{\gamma}{\omega_r\omega_*} \frac{dn_0}{dx}. \tag{38}$$

Since $\langle \tilde{v}_x^2 \rangle = \frac{1}{2}|\hat{v}_x|^2 = k_y^2|\hat{\phi}|^2/(2B^2)$, we have

$$\Gamma = -D\frac{dn_0}{dx}, \qquad D = \langle \tilde{v}_x^2 \rangle \frac{\gamma}{\omega_r\omega_*} \simeq \langle \tilde{v}_x^2 \rangle \frac{\gamma}{\omega_r^2}. \tag{39}$$

Using $\gamma/\omega_r = \delta$ and $\omega_r \simeq \omega_*$,

$$D = \langle \tilde{v}_x^2 \rangle \frac{\delta}{\omega_*} = \langle \tilde{v}_x^2 \rangle \sqrt{\frac{\pi}{2}} \frac{k_\perp^2\rho_s^2 - k_z^2 C_s^2/\omega_*^2}{|k_z| v_{\mathrm{t,e}}}. \tag{40}$$

For independent modes, cross terms between different (k_y, k_z) vanish under averaging over y and z, so their fluxes add directly:

$$\Gamma = -\left(\sum_k \langle \tilde{v}_x^2 \rangle_k \frac{\gamma_k}{\omega_{r,k}\omega_{*,k}}\right) \frac{dn_0}{dx}, \qquad \frac{\partial n_0}{\partial t} = -\frac{\partial \Gamma}{\partial x}. \tag{41}$$

III. NUMERICAL TESTS AND EXPERIMENTAL VALIDATION

Moving beyond the simpler slab-geometry drift-kinetic derivation in Section II, we now return to a more complete GK model for tokamaks and discuss its numerical and experimental validation.

A. Waltz 2009 (PoP 16, 072303)[6]

Waltz, Casati, and Staebler[6] test the quasilinear transport approximation (QLTA) itself by inserting the potential intensity spectrum of nonlinear GYRO simulations into the quasilinear flux formula. In the GA standard cases, the quasilinear diffusivities exceed the nonlinear ones by a nearly channel-independent factor: 1.4–1.8 for the mode form (mQLTA) and 1.2–1.4 for the frequency form (fQLTA). The approximation degrades at high $k_y\rho_s$, for strongly pinched particle flux, and, in the mode form only, for adiabatic-electron ITG turbulence far above threshold.

1. Formulation of the quasilinear tests

a. Fluxes. The flux-surface and time averaged ion energy, electron energy and particle fluxes, and the corresponding diffusivities, are defined by the correlation of the moment fluctuations with the radial $E\times B$ velocity:

$$\begin{aligned}[Q_i, Q_e, \Gamma] &\equiv \left[-n_i\chi_i\frac{dT_i}{dr}, -n_e\chi_e\frac{dT_e}{dr}, -D_e\frac{dn}{dr}\right] \\ &= \mathrm{Re}\sum_k \left\{[\delta E_{ik}^*, \delta E_{ek}^*, \delta n_k^*]\,\delta v_{Ek}\right\}^t,\end{aligned} \tag{42}$$

where

$$\delta v_{Ek} = \frac{c}{B}\, ik_y\,\delta\phi_k.$$

Here δE_{sk} is the energy-moment fluctuation of species s, $\{\cdots\}^t$ is the time average, the sum over k (toroidal mode number n, i.e. k_y) carries the flux-surface average, and a superscript (nl) marks fluctuations taken from a nonlinear simulation. Equation (42) is the multi-channel form of Eq. (11) (Gaussian units, c the speed of light).

b. Quasilinear weight and spectral weight. Every flux in Eq. (42) is bilinear in the fluctuations, so each wavenumber contribution factorizes as

$$\boxed{\Gamma_k = W_k^\Gamma\, S_k, \qquad W_k^\Gamma \equiv \frac{\mathrm{Re}\{\delta n_k^*\,\delta v_{Ek}\}}{\delta\phi_k^*\,\delta\phi_k}, \qquad S_k \equiv \{\delta\phi_k^*\,\delta\phi_k\}^t,} \tag{43}$$

and analogously for Q_i and Q_e with $\delta n_k \to \delta E_{sk}$. W_k is the *quasilinear weight* and $S_k = |\delta\phi_k|^2$ is the *spectral weight* (saturated potential intensity). The linearized gyrokinetic equations together with quasineutrality are homogeneous in the fluctuations: an eigenmode fixes the ratio $\delta n_k/\delta\phi_k$ (cross-phase and amplitude ratio) and leaves its overall amplitude free. W_k is therefore amplitude-independent and computable from linear theory, while S_k carries the nonlinear information. In

cross-phase form, with $\delta n_k/\delta\phi_k = |\delta n_k/\delta\phi_k|\, e^{-i\vartheta_k^n}$,

$$W_k^\Gamma = -\frac{ck_y}{B}\frac{|\delta n_k|}{|\delta\phi_k|}\sin\vartheta_k^n, \qquad \Gamma_k = -\frac{ck_y}{B}|\delta n_k||\delta\phi_k|\sin\vartheta_k^n, \tag{44}$$

so the quasilinear weight depends on both the cross-phase and the amplitude ratio. The opposite overall sign in Eq. (23) follows from the orientation of y there ($\hat{v}_x = -ik_y\hat{\phi}/B$).

The spectral weight appears as $I_k = |E_k|^2 = k^2|\phi_k|^2$ in the Vlasov quasilinear theory of Eq. (1), as $I_{k_y}^{QL}$ in the total quasilinear flux, and as $|\hat{\phi}|^2$ in the drift-wave flux Eq. (23). In the Vlasov problem the amplitude closes self-consistently through $dI_k/dt = 2\gamma_k[F]I_k$ with $\gamma_k \to 0$ at saturation. In gyrokinetic turbulence $t_{\rm nl} \ll t_{\rm eq}$, so S_k must be supplied externally: by a saturation rule such as that in QuaLiKiz, and by the nonlinear simulation itself in Waltz, Casati, and Staebler[6].

c. Linear response. Write the density response of species s as $\delta n_{s,k\omega} = R_{s,k}(\omega)\delta\phi_{k\omega}$. Its imaginary part gives the particle quasilinear weight:

$$W_{s,k}^\Gamma(\omega) = \frac{ck_y}{B}\,\mathrm{Im}\,R_{s,k}(\omega). \tag{45}$$

The in-phase adiabatic response contributes no flux; the non-adiabatic response supplies the cross-phase and amplitude ratio. Solving the linearized gyrokinetic equation and taking its density moment gives $R_{s,k}$; the response formula and intermediate algebra are collected in Appendix A.

d. Mode decomposition (mQLTA). [ZG] Each self-consistent linear eigenmode m has a complex frequency $\omega_k^m + i\gamma_k^m$. Evaluating the response at this frequency gives

$$W_{s,km}^\Gamma = \frac{ck_y}{B}\frac{e_s n_0}{T_s}\int d^3v\, F_0 J_0^2\,(\omega_{*s}^v - \varpi_s^v)\,\frac{\gamma_k^m}{(\varpi_s^v - \omega_k^m)^2 + (\gamma_k^m)^2}, \tag{46}$$

Here e_s is the signed charge, F_0 is a unit-normalized Maxwellian, J_0 accounts for gyroaveraging, ω_{*s}^v contains the equilibrium density and temperature gradients, and ϖ_s^v combines parallel motion and magnetic drift. Their explicit definitions are given in Eq. (A5). The flux is

$$\Gamma_s^{(\mathrm{mql})} = \sum_k\sum_m W_{s,km}^\Gamma S_{km}, \qquad S_{km} = \{\delta\phi_{km}^*\delta\phi_{km}\}^t. \tag{47}$$

The Lorentzian kernel connects this expression to the Vlasov diffusion coefficient derived after Eq. (1): kv is replaced by the particle frequency ϖ_s^v, and the drive comes from spatial gradients. The energy weight follows by taking the energy moment of the same response.

But mQLTA is overly simplistic, as it uses a single dominant mode weight for the entire intensity.[ZG]

e. Frequency decomposition (fQLTA). ZG Instead of assigning the field to linear eigenmodes, fQLTA evaluates the linear response to the full potential spectrum over real frequencies:

$$\Gamma_s^{(\mathrm{fql})} = \sum_k \int \frac{d\omega}{2\pi} W_{s,k}^{\Gamma}(\omega)\, S_k(\omega), \qquad W_{s,k}^{\Gamma}(\omega) = \frac{ck_y}{B}\,\mathrm{Im}\, R_{s,k}(\omega + i\varepsilon). \tag{48}$$

$$W_{s,k}^{\Gamma}(\omega) = \pi \frac{ck_y}{B}\frac{e_s n_0}{T_s} \int d^3v\, F_0 J_0^2\, (\omega_{*s}^v - \varpi_s^v)\, \delta(\omega - \varpi_s^v), \tag{49}$$

The real-frequency response selects resonant particles with $\omega = \varpi_s^v$. Thus mQLTA samples the response at discrete complex eigenfrequencies, whereas fQLTA convolves it with the complete prescribed frequency spectrum. The Fourier expansion, spectral normalization and resonance algebra are given in Appendix A.

f. Ambipolarity. In the electrostatic, quasineutral setting considered here, the shared $E \times B$ velocity and $\sum_s e_s \delta n_s = 0$ imply zero net radial charge flux, $\sum_s e_s \Gamma_s = 0$. For singly charged ions and electrons, this is $\Gamma_i = \Gamma_e$. In mQLTA, each self-consistent eigenmode satisfies the quasineutral dispersion relation, so

$$\sum_s e_s W_{s,km}^{\Gamma} = \frac{ck_y}{B}\,\mathrm{Im} \sum_s e_s R_{s,k}(\omega_k^m + i\gamma_k^m) = 0. \tag{50}$$

In fQLTA, each species responds independently to a prescribed potential, without imposing quasineutrality on the tracer density responses. Their particle fluxes therefore need not satisfy this constraint. In the kinetic-electron cases studied here, the electron response is closer to adiabatic and limits the plasma particle transport; the comparison therefore uses the electron tracer particle flux and discards the ion tracer channel.

2. Numerical implementation

a. Simulation set-up. All runs use GYRO in the local, electrostatic, collisionless limit with circular s-α geometry ($\alpha = 0$). The GA-ITG/TEM standard case has $q = 2$, $\hat{s} = d\ln q/d\ln r = 1$, $R/a = 3$, $r/a = 0.5$, $T_i/T_e = 1$, $n_i/n_e = 1$, $a/L_T = 3$, $a/L_n = 1$, with kinetic electrons at $\sqrt{M_i/m_e} = 60$. Variants are TEM1 ($a/L_T = a/L_n = 2$, ion and electron branches with nearly equal growth rates), TEM2 ($a/L_T = 1$, $a/L_n = 3$, TEM dominant at all $k_y\rho_s \leq 1$), and ITG-ae (adiabatic electrons). Diffusivities are in gyro-Bohm units $\chi_{\mathrm{gB}} = (c_s/a)\rho_s^2$, with $c_s = \sqrt{T_e/M_i}$, $\rho_s = c_s/\Omega_i$. Numerical grid and averaging details are given in Appendix B. The tests therefore cover ion-scale ITG/TEM turbulence at $\nu_* = 0$, $\beta = 0$ and zero rotation shear; ETG scales ($k_y\rho_s > 1$) are outside the grid.

b. Figure of merit: the overage. The overage is the ratio of quasilinear to nonlinear diffusivity in each channel,

$$O \equiv \left[\frac{\chi_i^{(\mathrm{ql})}}{\chi_i^{(\mathrm{nl})}}, \frac{\chi_e^{(\mathrm{ql})}}{\chi_e^{(\mathrm{nl})}}, \frac{D_e^{(\mathrm{ql})}}{D_e^{(\mathrm{nl})}} \right], \tag{51}$$

evaluated either in total or per wavenumber. The gradients are identical in both runs, so O is also the flux ratio. A transport model multiplies the spectral weight by one calibration coefficient C,

$$Q_i^{\mathrm{model}} = C \sum_k W_k^{Q_i} I_k, \qquad \Gamma^{\mathrm{model}} = C \sum_k W_k^{\Gamma} I_k \quad \Rightarrow \quad \frac{\Gamma^{\mathrm{model}}}{Q_i^{\mathrm{model}}} = \frac{\sum_k W_k^{\Gamma} I_k}{\sum_k W_k^{Q_i} I_k}, \tag{52}$$

so channel ratios are independent of C, and $C = 1/O$ corrects every channel at once when O is the same in all of them. The success criterion is therefore constancy of O across channels, wavenumbers and case parameters; the value $O > 1$ itself is absorbed into C.

c. mQLTA: two-step linear–nonlinear test. Step 1 is a linear GYRO run giving the quasilinear weight W_{k1} of the leading eigenmode at each k (the most unstable, outward ballooning mode, $\theta_0 = 0$). Step 2 is a nonlinear run giving the actual fluxes and the spectral weight. The full nonlinear intensity at each k is assigned to the leading mode,

$$\Gamma_{\mathrm{test}}^{(\mathrm{mql})} = \sum_k W_{k1}^{\Gamma} \{ \delta\phi_k^{*(\mathrm{nl})} \delta\phi_k^{(\mathrm{nl})} \}^t. \tag{53}$$

Subdominant branches and the continuum of less unstable ballooning modes ($\theta_0 \neq 0$), which carry smaller quasilinear weights and part of the spectral weight, are omitted; this biases O upward.

d. fQLTA: one-step plasma–tracer test. A direct two-step fQLTA test would require the linear response over all frequencies and the frequency-resolved nonlinear spectrum. Instead, each nonlinear run contains "plasma" ions and electrons at full density, which alone determine $\delta\phi^{(\mathrm{nl})}$, and identical "tracer" ions and electrons at negligible density, absent from the field equation. Two tracer variants are used:

1. Tracers with the nonlinear $E \times B$ term retained obey the same equation as the plasma species, so their diffusivities must equal the plasma ones. This verifies the method (Table II).

2. Tracers with the nonlinear $E \times B$ term deleted respond linearly to the full nonlinear potential $\delta\phi_k^{(\mathrm{nl})}(t)$. Their fluxes are the convolution Eq. (48) over the complete frequency spectrum, including subdominant modes and incoherent fluctuations, and define the fQLTA diffusivities.

The particle-channel comparison uses the electron tracer flux, as explained in the preceding discussion.

3. *Numerical results*

a. Standard cases. Table I lists the mQLTA overages. The mean over the nine entries is 1.64, and the normalized overages ($O/1.64$) scatter by 13.5% rms across the three kinetic-electron cases. The ITG-ae case gives $\chi_i^{(\mathrm{ql})}/\chi_i^{(\mathrm{nl})} = 6.24/3.76 = 1.66$, close to that mean. The sign of D_e in the pinched ITG/TEM case is reproduced.

Table I: mQLTA overages O (Eq. (51)) in the GA standard cases, from Waltz, Casati, and Staebler[6], Table I. Diffusivities in χ_{gB}; normalized overage $O/1.64$ in parentheses.

Case	$\chi_i^{(\mathrm{ql})}/\chi_i^{(\mathrm{nl})}$	$\chi_e^{(\mathrm{ql})}/\chi_e^{(\mathrm{nl})}$	$D_e^{(\mathrm{ql})}/D_e^{(\mathrm{nl})}$
ITG/TEM	$17.9/12.1 = 1.47$ (0.87)	$5.83/3.42 = 1.70$ (1.03)	$-3.21/-2.01 = 1.79$ (1.09)
TEM1	$21.8/15.0 = 1.45$ (0.88)	$21.0/15.3 = 1.37$ (0.84)	$7.86/5.50 = 1.42$ (0.87)
TEM2	$43.8/25.9 = 1.69$ (1.03)	$56.3/30.3 = 1.85$ (1.12)	$12.2/5.9 = 2.07$ (1.26)

Table II: Plasma–tracer tests in the ITG/TEM case, from Waltz, Casati, and Staebler[6], Tables II and III. Upper row: tracers with the nonlinear term retained. Lower row: nonlinear term deleted (fQLTA overage). The ion tracer particle channel is omitted as explained in the preceding discussion. The plasma values differ slightly between rows because of different grids and averaging windows.

Tracer	χ_i	χ_e	D_i	D_e
nonlinear (tr/nl)	12.0/12.0	3.22/3.28	$-2.03/-2.02$	$-2.01/-2.0$
linear (fQLTA)	$16.7/11.3 = 1.48$	$3.66/3.17 = 1.15$	discarded	$-2.7/-1.90 = 1.43$[a]

[a] Value as reported; the rounded entries give 1.42.

The fQLTA overages are smaller, as expected from Eq. (48): the spectral weight is shared with subdominant modes of smaller quasilinear weight.

b. Wavenumber dependence. Per-k overages grow at high $k_y\rho_s$ (Fig. 1). The spectral weight there is small, so the net overages change little. In the ITG/TEM case the jump above $k_y\rho_s \approx 0.5$ coincides with the transition from the ITG to the TEM branch. Waltz, Casati, and Staebler[6] attribute the high-k degradation to k^2D nonlinear resonance broadening.

Physical interpretation. For a given D, the decorrelation rate $k_\perp^2 D$ grows with wavenumber and can compete with the linear response, altering its phase.

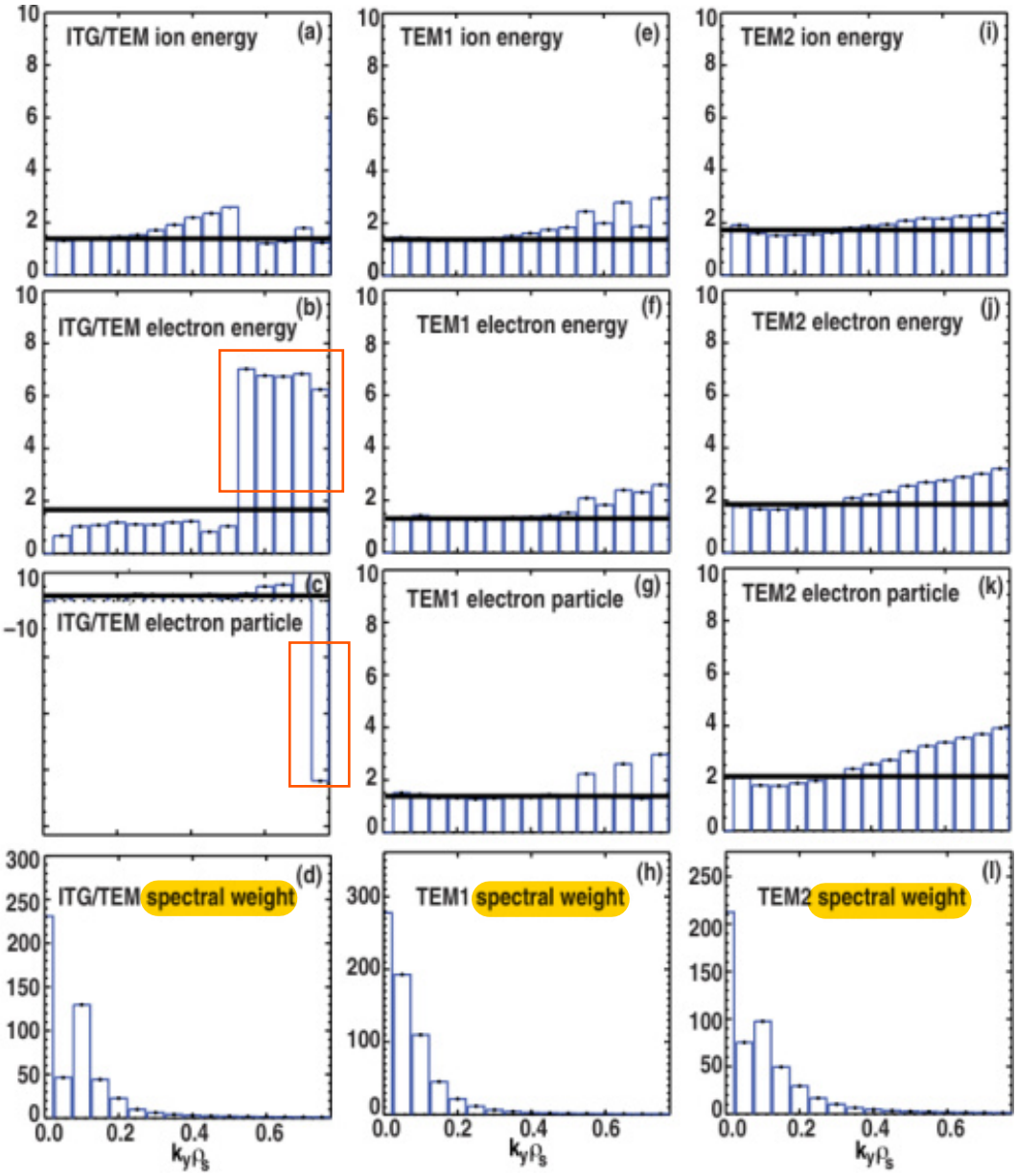

Figure 1: Per-wavenumber mQLTA overage for ion energy, electron energy and particle transport, and the nonlinear spectral weight, for the ITG/TEM, TEM1 and TEM2 cases. Horizontal lines mark the net overages of Table I. Adapted from Waltz, Casati, and Staebler[6], Fig. 1.

c. Tracer experiments. For the ion energy channel, the quasi-nonlinear and fQLTA tracer diffusivities add to the nonlinear value, $-4.83 + 16.7 = 11.87 \approx 11.3$; in the electron energy and particle channels the sum departs from the nonlinear value, which Waltz, Casati, and Staebler[6]

attribute to electron transport driven by the dominant low-k ITG turbulence. Mode deletion at $k_y\rho_s = 0.10$ and 0.60 leaves finite, purely nonlinearly induced transport at those wavenumbers.

d. Temperature-gradient scan: strongly pinched particle flux. In the ITG/TEM case with $2 < a/L_{T_i} = a/L_{T_e} < 9$ (Fig. 2), the energy-channel overages stay nearly constant (about 1.6 for mQLTA, 1.3 for fQLTA) while the energy transport rises four- to eight-fold. The particle overage separates from them, about threefold for mQLTA and twofold for fQLTA, and the mQLTA particle flux falls below the nonlinear value at $a/L_T = 2$. The cross-phase comparison (Fig. 3) locates the error: at low k, where most transport occurs, the linear density–potential cross-phase (positive, pinched) moves above the nonlinear distribution as a/L_T rises from 3 to 6, while the energy–potential cross-phases (negative, outward) track the nonlinear ones. Through Eq. (44) this error enters W_k^Γ directly. Mode deletion at $a/L_T = 9$ shows a larger share of nonlinearly induced transport in the pinched particle channel. For a modified TEM2 case with outward particle flux, the mQLTA overages remain nearly constant over the same scan (Waltz, Casati, and Staebler[6], Fig. 6).

Physical interpretation. The pinch is driven by the ITG branch and is the residual of inward (curvature pinch, thermodiffusion) and outward diffusive contributions; near cancellation makes Γ sensitive to small cross-phase errors, whereas the single-signed energy fluxes are robust. Waltz, Casati, and Staebler[6] describe these strong pinches as unrealistically large and note that the tokamak core usually operates near a weakly pinched, almost null particle flux. The calculation that decides the reliability of quasilinear density peaking predictions is the particle-channel overage at $\Gamma \approx 0$.

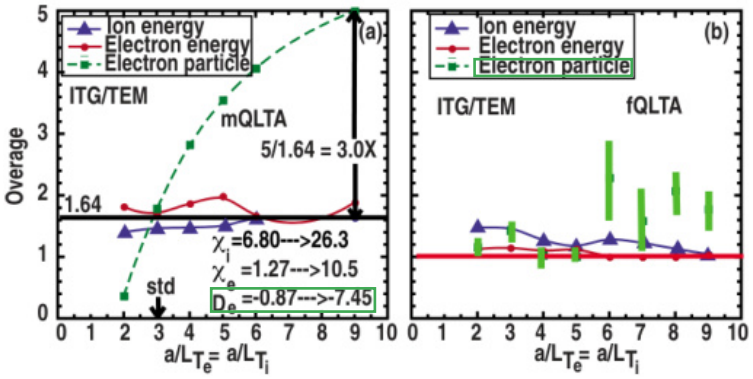

Figure 2: GYRO mQLTA and fQLTA overages versus a/L_T for the ITG/TEM case. Adapted from Waltz, Casati, and Staebler[6], Fig. 3.

在 $a/L_T=3$ 时，低波数处线性的密度 – 电势交叉相位（白线）落在非线性分布的峰上，约 0.1 rad；到 $a/L_T=6$ 时，白线移到约 0.3 – 0.5 rad，而非线性分布的峰仍在 0.1 rad 附近。
能量 – 电势交叉相位则在两种梯度下都约为 –1 rad，线性与非线性一致。

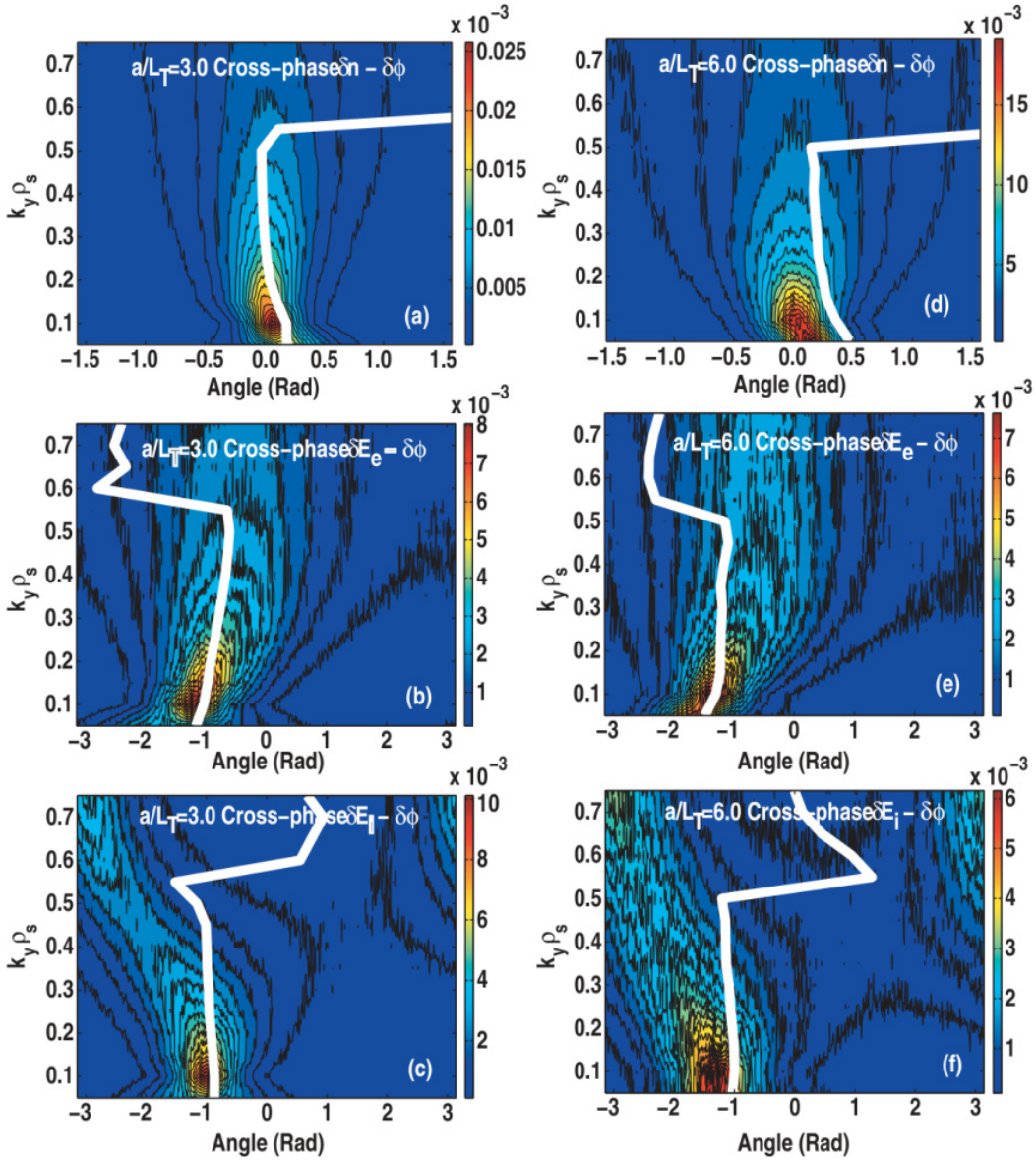

Figure 3: Linear cross-phase angles (lines) and probability density of the nonlinear cross-phase angles (contours) versus wavenumber for the particle, electron energy and ion energy channels, ITG/TEM case at $a/L_T = 3$ and 6. Adapted from Waltz, Casati, and Staebler[6], Fig. 5.

e. ITG-ae scan: amplitude-ratio failure. From $a/L_{T_i} = 3$ to 9, the mQLTA ion-energy overage rises 2.1-fold while the fQLTA overage stays nearly flat (Fig. 4). The linear pressure–potential cross-phase tracks the nonlinear one in this case, so the error lies in the amplitude ratio $|\delta p|/|\delta\phi|$ of Eq. (44). Preserving the linear cross-phase alone is therefore insufficient: the fluctuation-to-potential amplitude ratio must also remain representative of the nonlinear state.

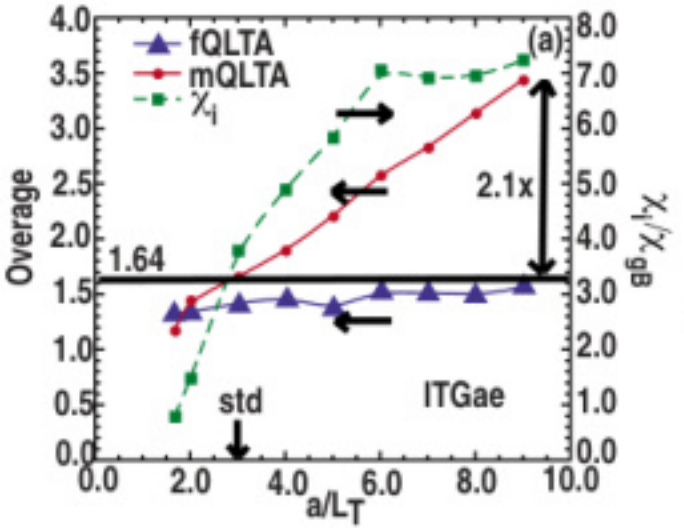

Figure 4: ITG-ae case versus a/L_{T_i}: fQLTA and mQLTA overages with the nonlinear $\chi_i/\chi_{\mathrm{gB}}$. Adapted from Waltz, Casati, and Staebler[6], Fig. 7(a).

f. Consequence for model building. Because these tests use the nonlinear spectral weight, the discrepancies diagnose errors in the quasilinear response rather than in a fitted saturation rule[6]. For these notes, the validity condition of Section I A becomes: nonlinear turbulence preserves both the cross-phases and the amplitude ratios of the linear eigenmodes. Waltz, Casati, and Staebler[6] show this for the energy channels at low $k_y\rho_s$ in the GA standard cases, with 13.5% channel-to-channel scatter of the normalized mQLTA overage.

The practical application of this framework is the prediction of core plasma profiles. Once the quasilinear weights are combined with a saturation prescription, the resulting turbulent fluxes can be coupled to transport equations, together with neoclassical transport, sources, and boundary conditions. The evolving profiles then determine the local gradients used in subsequent flux calculations[1]. The tests discussed here establish the usefulness and limitations of the quasilinear response for prescribed nonlinear fluctuation spectra. Predictive profile modelling additionally requires an accurate saturation model and validation against experimental measurements.[ZG]

B. Comparison of QuaLiKiz Model with Nonlinear Fluxes.

The quasilinear fluxes themselves, including the saturation rule, were extensively compared to nonlinear gyrokinetic simulations.

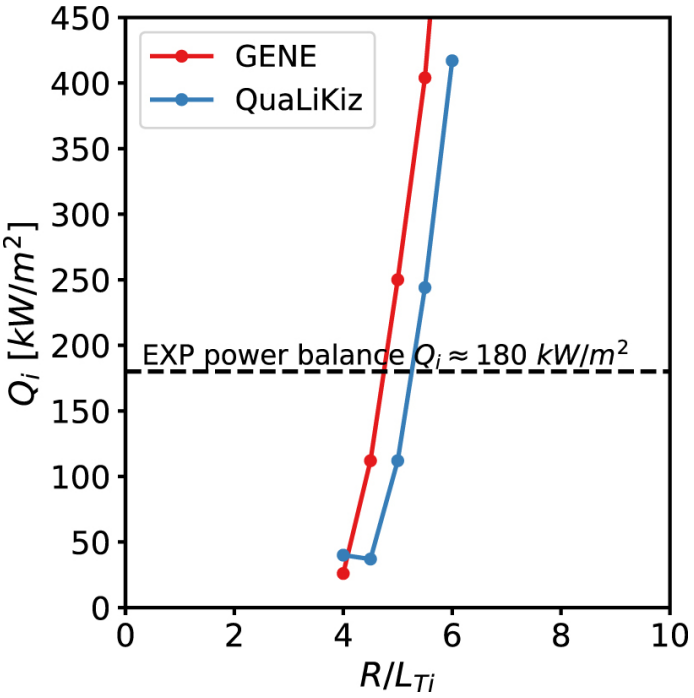

Figure 5: GENE nonlinear vs QuaLiKiz quasilinear flux comparison based on JET hybrid scenario 94875 at $\rho = 0.65$. Comparison was with $(\hat{s} - \alpha)$ geometry and without collisions. R/L_{Ti} leading to power-balance ITG turbulent fluxes agree within 10%, and the stiffness level set by the saturation rule agrees almost perfectly, while the QuaLiKiz calculations are$\sim \times 106$ faster. The QuaLiKiz residual flux near threshold far below power-balance is from TEM turbulence not predicted by GENE, but it is not experimentally relevant. Reproduced from Citrin *et al.* [7]

a. Experimental cross-phase validation. The measured n_e–T_e phase is consistent with nonlinear simulations, and the linear phase at the dominant transport scale also aligns with nonlinear results; thus, the experimental findings support the idea that the phase characteristics of linear modes are preserved within turbulence.

b. Core profile prediction. The JETTO code, coupled with QuaLiKiz, is used to predict the electron temperature and density profiles for JET baseline discharge 87412; these predictions are then compared with HRTS measurements, with the computational boundary set at $\rho = 0.85$.

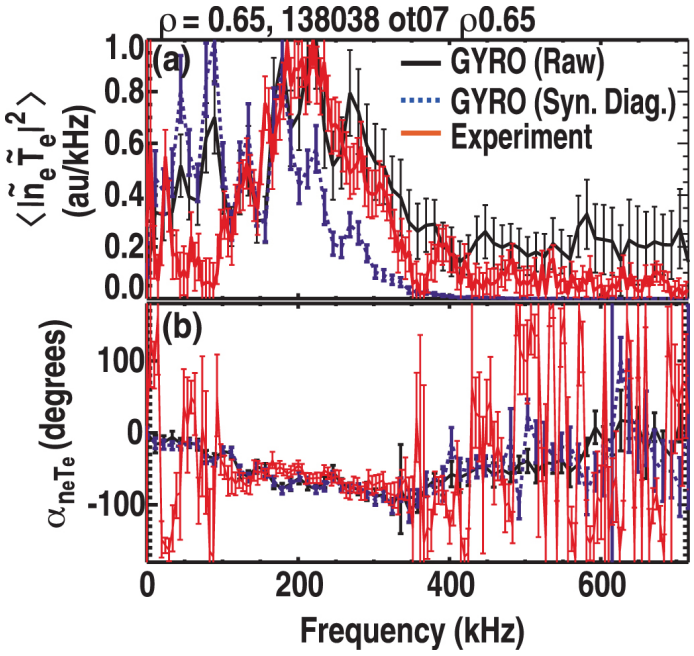

Figure 6: Comparison of experimental results at $\rho = 0.65$ to post experimental simulation results using the local parameters from DIII-D discharge 138038, $t = 1525$ ms as input. (a) The GYRO unfiltered (black-solid), synthetic diagnostic (blue-dashed), and experimental (red) cross-power spectra have been normalized to compare the spectral shape. (b) The GYRO unfiltered (black-solid), synthetic diagnostic (blue-dashed), and experimental cross-phase angles (red) are compared. The one-sigma standard deviations are plotted as error bars at each frequency in (a) and (b). Note that the experimental phase angle is meaningfully compared with the simulations only where it is resolved (frequencies where the coherency is high), between $90 < f < 350$ kHz. Outside this frequency range the measured $\alpha_{ne,Te}$ is in the noise. Reprinted from White *et al.* [8].

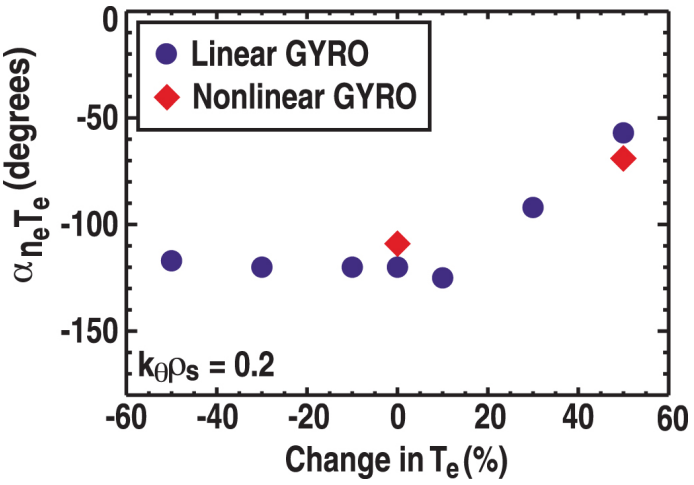

Figure 7: Figure 7. Values of electron density-temperature cross phase $\alpha_{ne,Te}$ at $k_y = 0.2$ vs percent change in Te. Linear GYRO runs (blue circles) and non-linear GYRO simulations (red diamonds) show good agreement for both the value of the cross phase and the trend with increasing Te. Reprinted from White *et al.* [8].

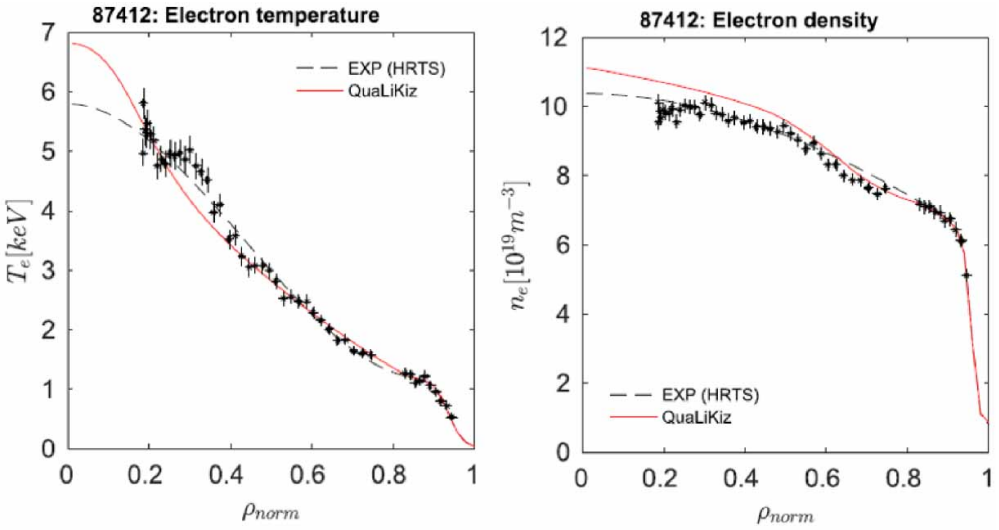

Figure 8: Comparison between JETTO+QuaLiKiz predictions for JET baseline scenario 87 412. The QuaLiKiz predicted and measured profiles HRTS are compared for electron temperature (left panel) and electron density (right panel). The QuaLiKiz boundary condition is at $\rho = 0.85$. Reproduced from Citrin *et al.* [9].

Appendix A: Derivation of the mode and frequency quasilinear weights

This appendix gives the intermediate steps behind the mQLTA and fQLTA expressions used in Section III A 1, following Waltz, Casati, and Staebler[6]. The final weights and flux formulas are retained in the main text.

1. Density response

After removing the collision term from Eq. (9), solve for $\tilde{g}_a$:

$$\tilde{g}_a = J_0 \frac{e_a \bar{\phi}}{T_a} F_a \frac{\omega - \omega_n - \omega_T (E/T - \frac{3}{2})}{\omega - u_\parallel \omega_{k\parallel} - u_\parallel^2 \omega_{d\parallel} - u_\perp^2 \omega_{d\perp}} \equiv J_0 \frac{e\phi}{T} F_0 \frac{\omega - \omega_*^v}{\omega - \varpi^v}. \tag{A1}$$

Substituting into Eq. (12), for $\delta\phi_k(t) = \delta\phi_{k\omega} e^{-i\omega t}$, the linear density response is[6]

$$\delta n_{k\omega} = n_0 \frac{e}{T} \delta\phi_{k\omega} \left\{ 1 - \int d^3v F_0(E) J_0^2(k_\perp \rho) \frac{\omega - \omega_{*k}^v}{\omega + i\varepsilon - \varpi_k^v} \right\}, \tag{A2}$$

$$\omega_{*k}^v = \frac{c k_y T}{eB} \left[\frac{1}{L_n} + \left(\frac{E}{T} - \frac{3}{2} \right) \frac{1}{L_T} \right], \qquad \varpi_k^v = k_\parallel u_\parallel + \omega_D, \tag{A3}$$

where F_0 is the Maxwellian in energy $E = mv^2/2$, J_0^2 is the double gyroaverage, ω_D is the curvature drift frequency and $\varepsilon \to 0^+$ enforces causality. The first term is the adiabatic response, in phase with $\delta\phi$; only the second (non-adiabatic) term contributes to W_k. Equation (A2) follows from solving the collisionless form of Eq. (9) for $\tilde{g}_a$ and inserting it into Eq. (12); in the slab limit $J_0 \to 1$, $\omega_D \to 0$, $L_T \to \infty$ it reduces to the drift-kinetic electron response Eq. (28).

2. From the response to the mode weight

To fix signs, write Eq. (A2) for species s with signed charge e_s as a response function $R_{s,k}$, in the orientation $\delta v_{Ek} = (c/B)\, i k_y \delta\phi_k$ of Eq. (42):

$$\delta n_{s,k\omega} = R_{s,k}(\omega)\, \delta\phi_{k\omega}, \qquad R_{s,k}(\omega) = -\frac{e_s n_0}{T_s} \left[1 - \int d^3v F_0 J_0^2 \frac{\omega - \omega_{*s}^v}{\omega - \varpi_s^v} \right], \tag{A4}$$

$$\omega_{*s}^v = \frac{c k_y T_s}{e_s B} \left[\frac{1}{L_n} + \left(\frac{E}{T_s} - \frac{3}{2} \right) \frac{1}{L_T} \right], \qquad \varpi_s^v = k_\parallel u_\parallel + \omega_{Ds}, \qquad \int d^3v F_0 = 1. \tag{A5}$$

For electrons ($e_s = -e$) in the slab limit ($J_0 \to 1$, $\omega_D \to 0$, $L_T \to \infty$), the velocity-space integrand of Eq. (A4) is the perturbed distribution of Eq. (28); the sign of ω_* differs from that equation only through the orientation of y.

Weight of one Fourier component. With $\delta n = R\,\delta\phi$,

$$\mathrm{Re}\{\delta n^*\,\delta v_E\} = \frac{ck_y}{B}\,|\delta\phi|^2\,\mathrm{Re}\{iR^*\} = \frac{ck_y}{B}\,|\delta\phi|^2\,\mathrm{Im}\,R, \tag{A6}$$

so the quasilinear weight is the imaginary part of the response. The adiabatic term in Eq. (A4) is real and drops out:

$$W^{\Gamma}_{s,k}(\omega) = \frac{ck_y}{B}\,\mathrm{Im}\,R_{s,k}(\omega) = \frac{ck_y}{B}\frac{e_s n_0}{T_s}\int d^3v\,F_0 J_0^2\,\mathrm{Im}\,\frac{\omega-\omega^v_{*s}}{\omega-\varpi^v_s}. \tag{A7}$$

The energy weight $W^{Q}_{s,k}$ follows from the energy moment, i.e. with a factor E inside the integral.

Normal modes. The potential at each k is expanded in linear normal modes m, each with a complex eigenfrequency $\omega^m_k + i\gamma^m_k$ that solves the quasineutral dispersion relation

$$\sum_s e_s R_{s,k}(\omega^m_k + i\gamma^m_k) = 0. \tag{A8}$$

Then

$$\delta\phi_k(t) = \sum_m \delta\phi_{km}\,e^{-i\omega^m_k t+\gamma^m_k t}, \qquad \delta n_{s,km} = R_{s,k}(\omega^m_k + i\gamma^m_k)\,\delta\phi_{km}. \tag{A9}$$

For $\gamma^m_k > 0$ the complex frequency itself supplies the causal prescription $\varepsilon \to \gamma^m_k$. Under the time average, cross terms between modes of different frequency vanish, and the growth factor $e^{2\gamma^m_k t}$ of each mode is replaced by its saturated intensity $S_{km} = \{\delta\phi^*_{km}\delta\phi_{km}\}^t$. With $\omega = \omega^m_k + i\gamma^m_k$ in Eq. (45) and the identity

$$\mathrm{Im}\,\frac{\omega_k + i\gamma_k - \omega^v_*}{\omega_k + i\gamma_k - \varpi^v} = \frac{\mathrm{Im}\big\{[(\omega_k-\omega^v_*)+i\gamma_k]\,[(\omega_k-\varpi^v)-i\gamma_k]\big\}}{(\varpi^v-\omega_k)^2+\gamma_k^2} = \frac{\gamma_k\,(\omega^v_*-\varpi^v)}{(\varpi^v-\omega_k)^2+\gamma_k^2}, \tag{A10}$$

one obtains the particle weight in Eq. (46). Substituting it into Eq. (47) gives the expanded flux:

$$\Gamma^{(\mathrm{mql})}_s = \sum_k\sum_m W^{\Gamma}_{s,km}S_{km} = \sum_k\sum_m \frac{ck_y}{B}\frac{e_s n_0}{T_s}S_{km}\int d^3v\,F_0 J_0^2\,(\omega^v_{*s}-\varpi^v_s)\,\frac{\gamma^m_k}{(\varpi^v_s-\omega^m_k)^2+(\gamma^m_k)^2}. \tag{A11}$$

For non-resonant particles, $|\varpi^v-\omega_k| \gg \gamma_k$, the kernel reduces to $\gamma_k/(\varpi^v-\omega_k)^2$, the structure of the drift-wave diffusivity $D \simeq \langle\tilde v_x^2\rangle\gamma/\omega_r^2$ obtained after Eq. (31). For weak turbulence ($\gamma_k \ll \omega_k$), a subdominant mode with smaller γ^m_k has a smaller quasilinear weight.

3. From the frequency spectrum to the resonant weight

The potential is instead expanded over real frequencies, each component acting as an external field on the linear response with $\varepsilon \to 0^+$:

$$\delta\phi_k(t) = \int\frac{d\omega}{2\pi}\,\delta\phi_{k\omega}e^{-i\omega t}, \qquad \delta n_{s,k}(t) = \int\frac{d\omega}{2\pi}\,R_{s,k}(\omega+i\varepsilon)\,\delta\phi_{k\omega}e^{-i\omega t}. \tag{A12}$$

For stationary turbulence, different frequencies are uncorrelated under the time average,

$$\{\delta\phi^*_{k\omega}\delta\phi_{k\omega'}\} = 2\pi\,\delta(\omega-\omega')\,S_k(\omega), \qquad \{\delta\phi^*_k\delta\phi_k\}^t = \int \frac{d\omega}{2\pi}\,S_k(\omega), \tag{A13}$$

so $S_k(\omega)$ is the frequency spectrum of the spectral weight, and Eq. (A6) applied component by component gives the convolution Eq. (48). For real ω, the factor $\omega-\omega^v_{*s}$ is real, and $1/(\omega+i\varepsilon-\varpi) = \mathscr{P}[1/(\omega-\varpi)] - i\pi\delta(\omega-\varpi)$ leaves only the resonant part:

$$\mathrm{Im}\,\frac{\omega-\omega^v_{*s}}{\omega+i\varepsilon-\varpi^v_s} = -\pi\,(\omega-\omega^v_{*s})\,\delta(\omega-\varpi^v_s) = \pi\,(\omega^v_{*s}-\varpi^v_s)\,\delta(\omega-\varpi^v_s). \tag{A14}$$

This gives the fQLTA weight in Eq. (49). The ω integral in Eq. (48) evaluates the spectrum at each particle's resonant frequency:

$$\Gamma^{(\mathrm{fql})}_s = \sum_k \frac{ck_y}{B}\frac{e_s n_0}{T_s}\int d^3v\,F_0 J_0^2\;(\omega^v_{*s}-\varpi^v_s)\,\tfrac{1}{2}\,S_k(\varpi^v_s). \tag{A15}$$

Transport comes only from particles with $\varpi^v_s=\omega$, and its sign is set by $\omega^v_{*s}-\varpi^v_s$ at resonance.

Appendix B: Numerical grid and averaging details

For the local GYRO tests described in Section III A 2, Waltz, Casati, and Staebler[6] use the following discretization and averaging parameters: $L_x = L_y = 126\rho_s$, $\Delta x = 0.75\rho_s$, 16 toroidal modes up to $k_y\rho_s = 0.75$, 12 parallel grid points, $8\times8\times2$ velocity points (energy, pitch angle, sign of $v_\parallel$), and time averages over 100–1000$\,a/c_s$. The physical case parameters and the restriction to ion-scale, electrostatic, collisionless turbulence are stated in the main text.

REFERENCES

[1] G. Staebler, C. Bourdelle, J. Citrin, and R. Waltz, Nucl. Fusion **64**, 103001 (2024).

[2] S. Brunner, E. Valeo, and J. A. Krommes, Physics of Plasmas **6**, 4504–4521 (1999).

[3] T. M. Antonsen and B. Lane, The Physics of Fluids **23**, 1205–1214 (1980).

[4] C. Bourdelle, X. Garbet, F. Imbeaux, A. Casati, N. Dubuit, R. Guirlet, and T. Parisot, in *Proceedings of the 34th EPS Conference on Plasma Physics*, Europhysics Conference Abstracts, Vol. 31F (Warsaw, Poland, 2007) pp. P–4.090.

[5] R. Goldston, *Introduction to Plasma Physics* (CRC Press, 1995).

[6] R. E. Waltz, A. Casati, and G. M. Staebler, Phys. Plasmas **16**, 072303 (2009).

[7]J. Citrin, S. Maeyama, C. Angioni, N. Bonanomi, C. Bourdelle, F. Casson, E. Fable, T. Görler, P. Mantica, A. Mariani, M. Sertoli, G. Staebler, and T. Watanabe, Nuclear Fusion **62**, 086025 (2022).

[8]A. E. White, W. A. Peebles, T. L. Rhodes, C. H. Holland, G. Wang, L. Schmitz, T. A. Carter, J. C. Hillesheim, E. J. Doyle, L. Zeng, G. R. McKee, G. M. Staebler, R. E. Waltz, J. C. DeBoo, C. C. Petty, and K. H. Burrell, Physics of Plasmas **17** (2010), 10.1063/1.3323084.

[9]J. Citrin, C. Bourdelle, F. J. Casson, C. Angioni, N. Bonanomi, Y. Camenen, X. Garbet, L. Garzotti, T. Görler, O. Gürcan, F. Koechl, F. Imbeaux, O. Linder, K. v. d. Plassche, P. Strand, and G. a. Szepesi, Plasma Physics and Controlled Fusion **59**, 124005 (2017).

[10]T. H. Dupree, Phys. Fluids **9**, 1773 (1966).

[11]W. Horton, Rev. Mod. Phys. **71**, 735 (1999).

[12]Z. Lin, I. Holod, L. Chen, P. H. Diamond, T. S. Hahm, and S. Ethier, Phys. Rev. Lett. **99**, 265003 (2007).

[13]A. Casati, C. Bourdelle, X. Garbet, F. Imbeaux, J. Candy, F. Clairet, G. Dif-Pradalier, G. Falchetto, T. Gerbaud, V. Grandgirard, Ö. D. Gürcan, P. Hennequin, J. Kinsey, M. Ottaviani, R. Sabot, Y. Sarazin, L. Vermare, and R. E. Waltz, Nucl. Fusion **49**, 085012 (2009).

[14]C. Bourdelle, X. Garbet, F. Imbeaux, A. Casati, N. Dubuit, R. Guirlet, and T. Parisot, Phys. Plasmas **14**, 112501 (2007).